 doi:10.20944/preprints202204.0161.v1

Article

Identification of Material Properties of Elastic Plate Using Guided Waves Based on the Matrix Pencil Method and Laser Doppler Vibrometry

Mikhail V. Golub [1], Olga V. Doroshenko[1], Mikhail A. Arsenov, Ilya A. Bareiko, Artem A. Eremin [1]*

[1] Institute for Mathematics, Mechanics and Informatics, Kuban State University, Krasnodar 350040, Russian Federation; m_golub@inbox.ru (M.V.G.); eremin_a_87@mail.ru(A.A.E.);
* Correspondence: m_golub@inbox.ru;

Abstract: Thin-walled structures inspection and damage detection often employs elastic waves, and demands accurate estimation of material properties. They require efficient automated techniques for data extraction and processing, which is still a challenging task. A advanced automated technique for material properties identification of an elastic waveguide is proposed in this investigation. The developed technique rely on the information on dispersion characteristics of guided waves, which are extracted applying the matrix pencil method to the measurements obtained via laser Doppler vibrometry. Two objective functions have been successfully tested, and advantages of both approaches are discussed (accuracy vs computational costs). The numerical analysis employing the synthetic data generated via the mathematical model as well as experimental data shows that both approaches are stable and accurate. The influence of the presence of certain mode in the extracted data is investigated. One can conclude that the influence of the corruptions related to the extraction of dispersion curves is not critical if the majority of guided waves propagating in the considered frequency range are presented. Possible extensions of the proposed technique for damaged and multi-layered structures are also discussed.

Keywords: laminate; material properties; identification; guided waves;

1. Introduction

Understanding of the behaviour of engineering structures is important equally at the stage of its manufacturing and design (e.g. for novel materials and for quality control) as well as at the operation stage (damage detection). Besides, accurate identification of material properties are critical for numerical models, where discrepancies between assumed and actual values of parameters may cause large errors in the prediction and may, therefore, lead to catastrophic failures. Various static or dynamic methods are used to determine the elastic constants of materials [1–3]. The static experiments include tensile, compression and bending tests, whereas dynamic methods include various low-frequency and high-frequency approaches. In general, dynamic tests are superior over static tests in determining the elastic constants since the dynamic tests are far below the elastic limit [4].

The advancement of experimental facilities and devices last decades caused the intensive development of non-destructive dynamic approaches for material characterization. Non-destructive dynamic identification techniques have evident advantages, they are usually cheaper, more rapid and accurate compared to static approaches. Detailed reviews of the non-destructive vibrational evaluation methods, where low frequencies are employed, can be found in [3,5]. Guided waves based material properties identification techniques rely on wave propagation characteristics, which carry on information on the material properties in a wider frequency range compared with vibrational evaluation methods. Therefore, they require multi-modal high-resolution signals, where

data extraction and extraction for multiple propagating modes is necessary, which is still a challenging task [6]. Scanning of the certain area of specimen is necessary to obtain dispersion properties, and, therefore, various experimental techniques are used. Chen *et al.* [6], Okumura *et al.* [7,8], Bochud *et al.* [9] and many others used linear array probe attached at the surface of a specimen for dispersion data extraction. Since attachment of an ultrasonic probe changes guiding properties of the waveguide in the area of contact, non-contact techniques are preferable. The waveguide characteristics are also often measured by a laser ultrasonics technique: waves are excited by a laser source through thermoelastic conversion [] **[AAE]** or by a piezoelectric transducer [10–12] and surface displacement/velocity is detected by laser interferometry. , A scanning procedure can be also performed by an air-coupled transducer, e.g. Takahashi *et al.* [13] varied angle of incidence, in order to estimate properties of a bi-layered structure. Also, the non-contact technique based on the transient grating method was employed for identification of elastic properties of a composite consisting of GaN nanowires embedded into a dielectric matrix [14].

Waveguide characteristics are obtained via the minimization of the discrepancy between the measured and calculated wave characteristics. Therefore, an optimization problem is to be solved, where an objective function providing a stable numerical procedure fitting a waveguide model to the experimental data should be constructed. In vibrational material identification, the objective function can generally be defined in various forms involving natural frequencies and mode shapes [5]. For instance, Pagnotta and Stigliano [15] investigated the feasibility of vibration based approach using natural frequencies of thin isotropic plates of any shape to determine their Young's modulus, Poisson ratio, mass density and thickness, and showed the robustness of the identification process with respect to measurement noise was also assessed. As soon as measurements are made, the characteristic features (wavenumbers, velocities or slownesses) are to be accurately extracted from the experimental data. For this purpose, the two-dimensional Fourier transform [9,10,14,16], the dynamic mode decomposition [17] or the matrix pencil method (MPM) [18–20].

The characteristic features of guided waves (GWs) obtained from the experiment are further used for the inverse problem solution, which also involve intensive computations using mathematical models [9,14,20,21]. In GW-based identification methods, various objective functions are constructed employing dispersion characteristics. A popular approach is to consider discrepancy between experimental and theoretical wavenumbers or phase velocities of GWs [13]. The latter demands calculation of dispersion curves of a waveguide, but the latter is reduced to root-finding procedures, which are cumbersome for multi-layered waveguides. Besides, mode separation and reconstruction method to extract individual modes from dispersive multi-modal GWs is needed [22]. Fairuschin *et al.* [23] used a different method, in which the dispersion properties are calculated solving the underlying differential equations using the spectral collocation method. The latter provides a good trade-off between precision, implementation effort, and computation, but it is not always robust [24]. It should be mentioned that additional features of GWs such as zero group velocities can be combined with waveguide modelling for material properties identification. [25].

Alternative approaches avoiding root-finding procedures, which are time-consuming, rely also on dispersion characteristics. Thelen *et al.* [21] proposed a thorough assessment of the effective mechanical behaviour of pSi using dispersion maps, where the maps are obtained by converting the modelled guided modes into a binary image. The objective function is defined as the mean value of the element-wise product between experimental and modelled dispersion maps. Chen *et al.* [6] and Bochud *et al.* [9] defined the objective function as the ratio of the number of experimental pairs wavenumber-frequency estimates satisfying the dispersion equation to the number of the total estimates for an isotropic layer. In this case, roots of the dispersion equation are not necessary, since the experimental wavenumber-frequency are substituted into the dispersion equation,

Preprints (www.preprints.org) | NOT PEER-REVIEWED | Posted: 18 April 2022 doi:10.20944/preprints202204.0161.v1

and the objective function is defined using signum function showing sign changes near certain wavenumber at a given frequency, for more details see [6,9]. Also, Green's matrices can be employed instead of the dispersion equation [14,26], which demands more computational time (2-3 times), but provides a smoother objective function.

In this paper, a novel automated technique for material properties identification of an elastic waveguide is proposed, validated and verified using synthetic and experimental data. The approach rely on the information on dispersion characteristics of guided waves, which are extracted here applying the matrix pencil method to the measurements obtained via laser Doppler vibrometry. Two objective functions have been composed: the first functional uses information on slownesses, while the second one employs the Fourier transform of Green's matrix [14]. The numerical analysis employing the synthetic data generated via the mathematical model (the algorithm of data synthesis is described in Section 5) shows that both approaches are stable and accurate. It demonstrated that the approach using slownesses is more accurate, but it is more time consuming. The influence of the presence of certain mode in the extracted data is investigated. One can conclude that the influence of the corruptions related to the extraction of dispersion curves extraction is not critical if the majority of guided waves propagating in the considered frequency range are presented. Discussions of the possible extensions of the proposed technique for damaged and multi-layered structures are also given.

2. Experimental data extraction using the matrix pencil method

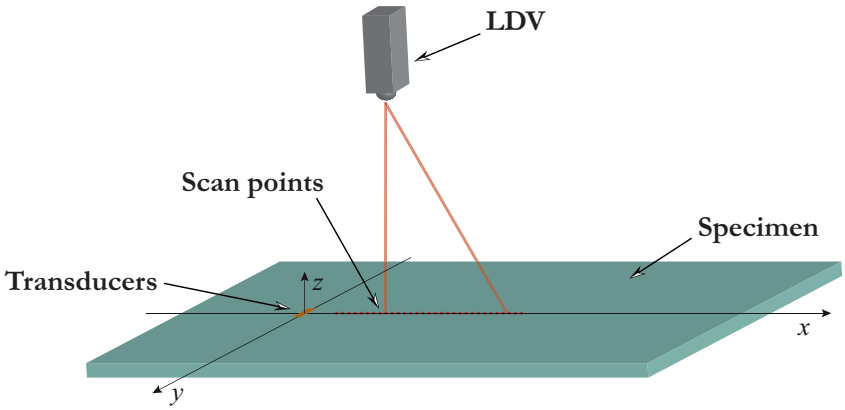

Figure 1. Experimental setup

Ultrasonic GWs are excited in the rectangular plate by a circular piezoelectric actuator of 5 mm radius and 0.5 mm thickness manufactured from PZT PIC 151 (PI Ceramic GmbH, Germany). Out-of-plane velocities of propagating wave packages are measured at the surface of the specimen by PSV-500-V laser Doppler vibrometer (LDV) (Polytec GmbH, Germany), which head is placed about 1100 mm above the sample minimizing the oblique angle laser beam measurement errors [**?**]. Since the specimen surfaces remained intact with no special treatment for their reflectivity improvement applied, at least 200 times averaging are performed for each measurement point to improve the signal-to-noise ratio. The experimental setup is schematically shown in Figure 1. The actuator was driven by broadband 0.5 μs rectangular pulse tone burst voltage, which spectrum is non-zero for the frequencies up to 3 MHz.

For the sake of convenience, let us introduce the Cartesian coordinates so that the scan line goes along the Ox-axis, and the transducer is situated at the origin of coordinates. The LDV allows measuring out-of-plane velocities $v(x, 0, 0, t)$ at the surface $z = 0$ of the specimen.

The out-of-plane velocities $v(x_i, t_k) = v_{ik}$ measured at points $(x_i, 0, 0)$ at moments of time t_k can be evaluated using the matrix pencil method (MPM). According to the MPM, the Fourier transform is applied to $v(x_i, t_k)$ with respect to time-variable for a

Preprints (www.preprints.org) | NOT PEER-REVIEWED | Posted: 18 April 2022 doi:10.20944/preprints202204.0161.v1

certain set of frequencies f_j, which gives $V(x_i, f_j) = V_i^j$. The MPM, where the singular value decomposition is applied to $V(x_i, f_j)$ for computing the discrete relation between the wavenumber k and the frequency f following Schöpfer *et al.* [18]. Thus, a set of slownesses s_{ij} of some guided waves propagating at frequency f_j are determined after the application of the processing procedure, which deletes noise and the results of the MPM, which do not correspond to a propagating guided wave. Therefore, some guided waves are not included in the final set and vice versa, some s_{ij} do not match the actual guided wave.

3. Theoretical determination of guided waves characteristics

Figure 2. Geometry of the problem

Let us consider steady-state motion of an elastic layer $V = \{|x| < \infty, -H \le z \le 0\}$ of thickness H characterized by the mass density ρ, Young's modulus E and Poisson's ratio ν as shown in Figure 2, so that parameter of the model $\boldsymbol{\theta} = \boldsymbol{\theta} = \{E, \nu, H\}$ is introduced. For the time-harmonic wave motion with the angular frequency $\omega = 2\pi f$, the displacement vector $\boldsymbol{u}$ obeys the Lame equation

$$\frac{1-\nu}{1-2\nu}\nabla\cdot\nabla\boldsymbol{u} - \frac{1}{2}\nabla\times(\nabla\times\boldsymbol{u}) + \frac{(1+\nu)\rho}{E}\omega^2\boldsymbol{u} = \boldsymbol{0}. \tag{1}$$

The Hooke's law relates the components of the stress tensor σ_{ik} and the displacement vector $\boldsymbol{u}$. The upper and lower surfaces of the layer are assumed to be stress-free

$$\sigma_{i2}(x,0) = \sigma_{i2}(x,-H) = 0, \qquad \forall x. \tag{2}$$

Since the solution corresponding to a guided wave propagating in a positive direction with the wavenumber ζ at the angular frequency $\omega = 2\pi f$ (f is the dimensional frequency) has the form:

$$\boldsymbol{u}(x,z,\omega) = \boldsymbol{U}(z)\exp(\mathrm{i}\zeta x - \mathrm{i}\omega t).$$

The latter form is substituted into governing equations (1), which leads to the following system of ordinary differential equations:

$$\mathbf{B}_2(\zeta)\frac{\mathrm{d}^2\boldsymbol{U}(z)}{\mathrm{d}z^2} + \mathbf{B}_1(\zeta)\frac{\mathrm{d}\boldsymbol{U}(z)}{\mathrm{d}z} + \omega^2\mathbf{B}_0(\zeta)\boldsymbol{U}(z) = \boldsymbol{0}. \tag{3}$$

Differential equations (3) can be rewritten in the following form

$$\frac{\mathrm{d}^2\boldsymbol{Y}}{\mathrm{d}z^2} = \mathbf{P}(\zeta, f)\boldsymbol{Y}, \tag{4}$$

$$\boldsymbol{Y} = \left\{U_1, U_2, \frac{\partial U_1}{\partial z}, \frac{\partial U_2}{\partial z}\right\}.$$

The solution of (4) can be written in terms of the matrix $\mathbf{M}(\zeta, f)$ composed of eigenvectors and $\mathbf{E}(\zeta, f, z) = \mathrm{diag}\{\exp(\gamma_1 z), \ldots, \exp(\gamma_4 z)\}$, where $\gamma_1(f)$ are eigenvalues of $\mathbf{P}(\zeta, f)$:

$$\boldsymbol{Y}(\zeta, f, z) = \mathbf{M}(\zeta, f)\cdot\mathbf{E}(\zeta, f, z)\cdot\boldsymbol{t}. \tag{5}$$

Preprints (www.preprints.org) | NOT PEER-REVIEWED | Posted: 18 April 2022 doi:10.20944/preprints202204.0161.v1

Replacement of (5) into stress-free boundary conditions (2) gives

$$\mathbf{T}(\zeta)\cdot\mathbf{M}(\zeta,f)\cdot\mathbf{E}(\zeta,f,0)\cdot\boldsymbol{t}=\mathbf{0},$$
$$\mathbf{T}(\zeta)\cdot\mathbf{M}(\zeta,f)\cdot\mathbf{E}(\zeta,f,-H)\cdot\boldsymbol{t}=\mathbf{0},$$

which can be rewritten in terms of four-by-four matrix $\mathbf{D}$

$$\mathbf{D}(\zeta,f)\cdot\boldsymbol{t}=0 \tag{6}$$

and differential operator $\mathbf{T}(\zeta)$ corresponding to the Hooke's law. Therefore, the solution $\zeta_k(f)$ of the dispersion relation

$$\Delta(f,\zeta_k)=\det\mathbf{D}(\zeta_k,f)=0 \tag{7}$$

gives wavenumbers of guided waves propagating in the elastic layer. In order to construct components of the Fourier transform of Green's matrix $\mathbf{K}_{ij}(\zeta,f)$, the right-hand side of the system (6) is substituted by $\boldsymbol{g}_j$ ($\boldsymbol{g}_1=\{1,0,0,0\}^{\mathrm{T}}$, $\boldsymbol{g}_2=\{0,1,0,0\}^{\mathrm{T}}$) assuming that the load is applied at the lower boundary $z=0$. The latter leads to the following system:

$$\mathbf{D}(\zeta,f)\cdot\boldsymbol{t}_j=\boldsymbol{g}_j. \tag{8}$$

The solution of (8) is then substituted into (5), and the Fourier transform of Green's matrix can be represented as follows

$$\boldsymbol{K}(f,\zeta/f,z,\boldsymbol{\theta})=\mathbf{M}(\zeta,f)\cdot\mathbf{E}(\zeta,f,z)\cdot\{\boldsymbol{t}_1(\zeta,f),\boldsymbol{t}_2(\zeta,f)\} \tag{9}$$

in terms of slowness value $s(\boldsymbol{\theta})=\zeta(\boldsymbol{\theta})/f$, which is employed further.

4. Objective functions for material properties characterization

As soon as slownesses $\check{s}_k$ at frequencies f_n ($n=\overline{1,N_f}$) are extracted from the experimental data, an inverse problem for material properties' identification is to be formulated and solved. With a certain model parameter vector $\boldsymbol{\theta}$ including Young's modulus, Poisson's ratio and plate thickness, the mathematical model presented in Section 3 can be applied for computing slownesses as roots of dispersion equation (7) (for instance, using the method of interval bisection) or the Fourier transform of Green's matrix (9). Numerical routines for calculating slownesses s and the Fourier transform of Green's matrix (9) at a given frequency f have been implemented in the FORTRAN programming language. Therefore, an inverse problem is settled matching the experimental and theoretical results via a specially composed objective function. Two main approaches for the objective function composition are considered here, and the effectiveness of several kinds of objective functions for material properties identification are compared in subsequent sections.

For both approaches and all the objective functions, the following optimization problem is formulated

$$\hat{\boldsymbol{\theta}}=\arg\min_{\boldsymbol{\theta}\in\Theta}g(\boldsymbol{\theta},\check{\boldsymbol{\theta}}).$$

Here Θ denotes the bounds of the model parameters of a certain objective function $g(\boldsymbol{\theta},\check{\boldsymbol{\theta}})$, where the unknown parameter $\check{\boldsymbol{\theta}}$ incorporates information on the actual value of the parameter, and $\hat{\boldsymbol{\theta}}$ is an estimate determined as a result of solving the optimization problem. The solution of the optimization problem has been implemented in the Python programming language using the Broyden-Fletcher-Goldfarb-Shanno (BFGS) method.

4.1. Objective function using residual of slownesses

In the first approach, the multi-parameter criterion is the minimization of the residual between measured slownesses $\check{s}_k$ and slownesses s_k caclulated employing mathematical model with parameters $\boldsymbol{\theta}$. Therefore, an iterative correction of simulation

Preprints (www.preprints.org) | NOT PEER-REVIEWED | Posted: 18 April 2022 doi:10.20944/preprints202204.0161.v1

results is to be performed varying material properties $\boldsymbol{\theta}$ until the optimal match between slowness-frequency pairs $(s_k(\boldsymbol{\theta}, f_n), f_n)$ calculated using a theoretical model with parameters $\boldsymbol{\theta}$ and the experiment $(\check{s}_k(\check{\boldsymbol{\theta}}, f_n), f_n)$, which contain information about the unknown parameter vector $\check{\boldsymbol{\theta}}$, as well as other factors affecting the experiment. Experimentally determined slownesses are denoted as $\check{s}_k(\check{\boldsymbol{\theta}}, f_n)$ to show straightforwardly that information about actual material properties $\check{\boldsymbol{\theta}}$ is included into the data.

Formally, the optimal model parameters $\hat{\boldsymbol{\theta}}$ are obtained from the minimization of the objective function

$$F(\boldsymbol{\theta}, \check{\boldsymbol{\theta}}) = \frac{1}{N} \sum_{n=1}^{N_f} \sum_{k \in \mathcal{P}_n} |\check{s}_k(\check{\boldsymbol{\theta}}, f_n) - s_k(\boldsymbol{\theta}, f_n)| \tag{10}$$

is composed assuming the modal decomposition of the data. Here, k is the index of experimentally found out data for some frequency f_n, i.e. $\mathcal{P}_n = \{k | \exists \check{s}_k(\check{\boldsymbol{\theta}}, f_n), n = \overline{1, N_f}\}$, N_f is the number of all frequencies, and N is the total number of pairs. Weights can also be used to take into account the sensitivity of the modes to the material properties changes, while such investigation is out of the scope of the present study and the weights are assumed to be equal. The disadvantage of the employment of this objective function is the necessity of the numerical search of the roots of dispersion equation (7) for all dissimilar frequencies $\check{s}_k(\check{\boldsymbol{\theta}}, f_n)$ and the determination of slownesses $s_k(\boldsymbol{\theta}, f_n)$ corresponding to experimental ones.

4.2. Objective function based on the Fourier transform of Green's matrix

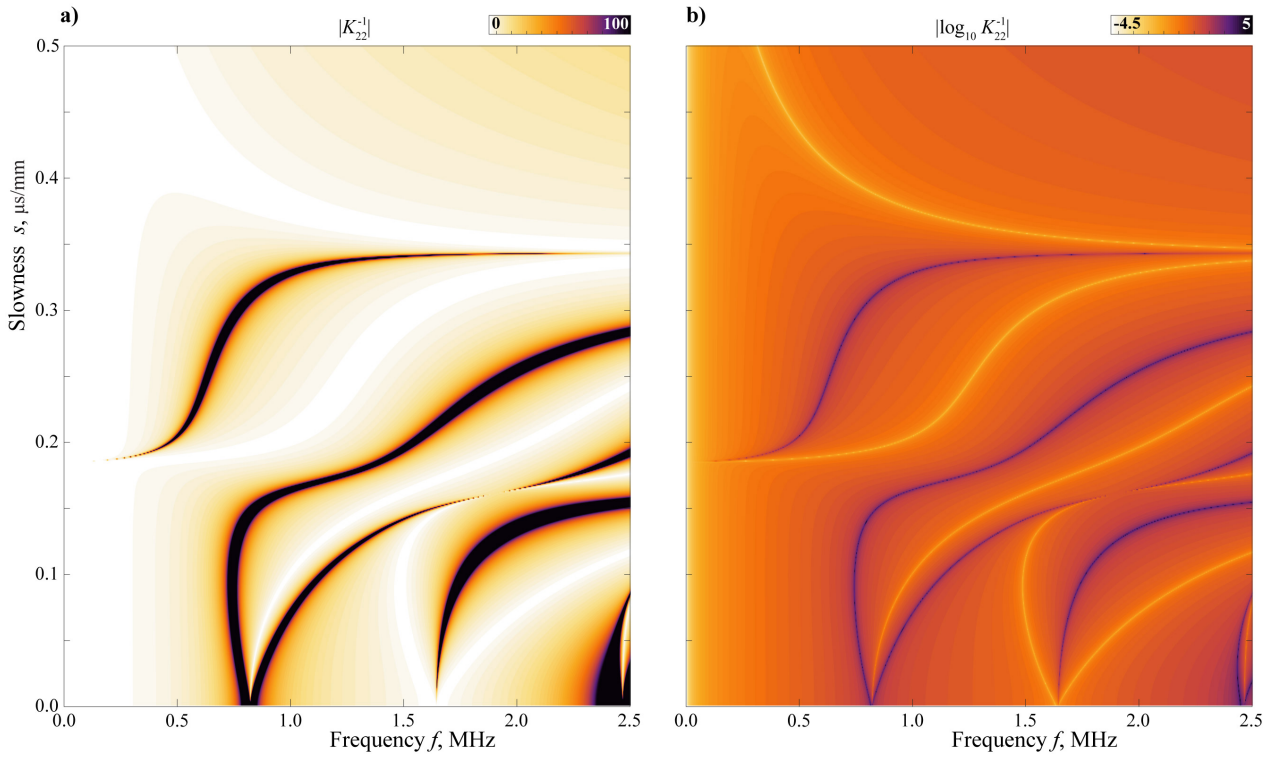

Figure 3. Surfaces of dispersion maps for $|K_{22}^{-1}(f, s, 0, \boldsymbol{\theta})|$ (a) and $\log_{10}|K_{22}^{-1}(f, s, 0, \boldsymbol{\theta})|$ (b) at $\boldsymbol{\theta} = \{70\text{ GPa}, 0.33, 1.9\text{ mm}\}$.

The second approach avoids time-consuming root search procedure. Moreover, instead of direct insertion of the experimentally determined slowness-frequency pairs $(\check{s}_k(\check{\boldsymbol{\theta}}, f_n), f_n)$ into dispersion equation (7), they are substituted into the inversion of the Fourier transform of Green's matrix $K_{22}^{-1}(f, s, 0, \boldsymbol{\theta})$ as proposed in [26]. The latter provides a smoother surface compared with $\Delta(f, s)$, an example of dispersion map

Preprints (www.preprints.org) | NOT PEER-REVIEWED | Posted: 18 April 2022 doi:10.20944/preprints202204.0161.v1

$|K_{22}^{-1}(f,s,0,\boldsymbol{\theta})|$ is demonstrated in Figure 3a for typical aluminium parameters $\boldsymbol{\theta} = \{70\text{ GPa}, 0.33, 1.9\text{ mm}\}$ (here all values $|K_{22}^{-1}(f,s,0,\boldsymbol{\theta})| > 100$ are substituted by 100). In this case, the following objective function is employed:

$$G_\beta(\boldsymbol{\theta},\check{\boldsymbol{\theta}}) = \frac{1}{N}\sum_{n=1}^{N_f}\sum_{k\in\mathcal{P}_n}\min\Big(|K_{22}^{-1}(f_n,\check{s}_k(\check{\boldsymbol{\theta}},f_n),0,\boldsymbol{\theta})|,\beta\Big). \tag{11}$$

Here, an additional parameter β is introduced in order to avoid large values of objective function (11), which improves the effectiveness of the inversion procedure, since extremely large values (they are visible in Figure 3b) could strongly influence on the objective function, if, for instance, some points related to noise are included. Another alternative for avoiding too large values of the objective function is the employment of a logarithm procedure so that objective functions

$$H_\beta(\boldsymbol{\theta},\check{\boldsymbol{\theta}}) = \frac{1}{N}\sum_{n=1}^{N_f}\sum_{k\in\mathcal{P}_n}\ln\min\Big(|K_{22}^{-1}(f_n,\check{s}_k(\check{\boldsymbol{\theta}},f_n),0,\boldsymbol{\theta})|,\beta\Big)$$

and

$$J_\beta(\boldsymbol{\theta},\check{\boldsymbol{\theta}}) = \frac{1}{N}\sum_{n=1}^{N_f}\sum_{k\in\mathcal{P}_n}\log_{10}\min\Big(\Big|K_{22}^{-1}(f_n,\check{s}_k(\check{\boldsymbol{\theta}},f_n),0,\boldsymbol{\theta})\Big|,\beta\Big),$$

which are also considered in this study. An example of dispersion map $\log_{10}|K_{22}^{-1}(f,s,0,\boldsymbol{\theta})|$ is shown in Figure 3b for the same parameters $\boldsymbol{\theta}$ as used for Figure 3a.

5. Generation of test data sets

In the case of the data obtained from a physical experiment, slownesses can be represented as a sum of the slownesses depending on the material parameters and the random component ϵ included the actions of random factors during the experiment, which can be represented as follows for a given discrete data set

$$\check{s}_k(\check{\boldsymbol{\theta}},f_n) = s_k(\check{\boldsymbol{\theta}},f_n) + \varepsilon_{nk}.$$

To obtain statistics proving the effectiveness of the identification procedure, the method must be validated in numerous tests, where the material properties $\check{\boldsymbol{\theta}} \in \Theta$ are known, but the data have to simulate experimental data. For this purpose, test data sets, i.e. slowness-frequency pairs, are to be prepared at first.

At the first stage of the test data preparation, theoretical slownesses are calculated for a known parameter $\check{\boldsymbol{\theta}} = \boldsymbol{\theta}^*$ at the set of frequencies $\{f_n'\}_{n=1}^{N'}$. Since the number of propagating guided waves varies with frequency, slowness-frequency pairs are split into sets $s_k(\boldsymbol{\theta}^*,f_n')$ of various numbers of elements M_k' in the general case, and each set corresponds to a kth non-attenuating guided wave. Next, white noise $\check{\epsilon} \sim N(0,\sigma)$ with the standard deviation σ is added so that

$$s_k'(\boldsymbol{\theta}^*,f_n') = s_k(\boldsymbol{\theta}^*,f_n')(1+\check{\epsilon})$$

is generated independently, and corrupted data sets $(s_k'(\boldsymbol{\theta}^*,f_n'),f_n'\})$ are prepared for each guided wave.

At the next stage, the noisy slownesses $s_k'(\boldsymbol{\theta}^*,f_n')$ are damaged for getting a given percentage δ of gaps in the dispersion curves. To this end, the parameter $\delta_1 \in (0,1]$ describing the percentage of sole points to be removed from initial data and the parameter $\delta_2 \in (0,1]$ describing percentage of points belonging to chains of lengths from 2 to 7 to be deleted from $s_k'(\boldsymbol{\theta}^*,f_n')$ are introduced so that $\delta = \delta_1 + \delta_2 < 1$.

Preprints (www.preprints.org) | NOT PEER-REVIEWED | Posted: 18 April 2022 doi:10.20944/preprints202204.0161.v1

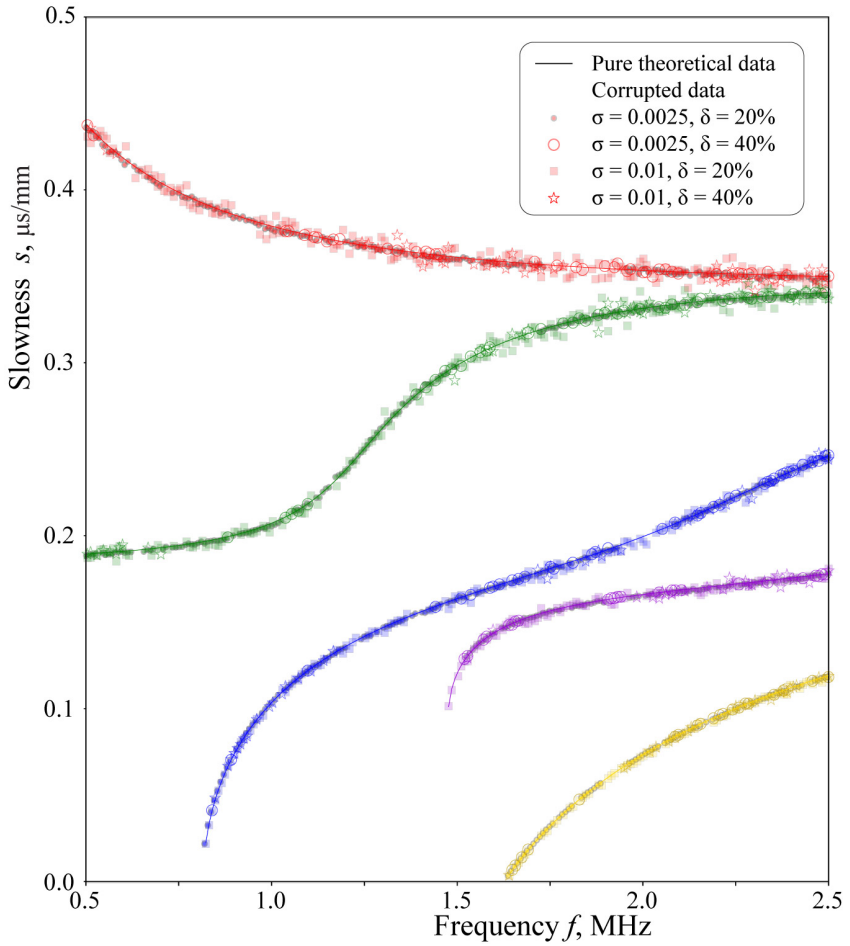

Figure 4. Examples of artificially generated corrupted slowness-frequency pairs $(\check{s}_k(\boldsymbol{\theta}^*, f_n), f_n)$ for $\boldsymbol{\theta}^* = \{70\,\text{GPa}, 0.33, 1.9\,\text{mm}\}$.

For simplicity, let us introduce one-dimensional arrays of frequencies related to kth guided wave as follows:

$$\{f'_{nk}\} = \{f'_n \,|\, \operatorname{Im} s'_k(\boldsymbol{\theta}^*, f'_n) = 0\}.$$

and denote their lengths as $M'_k = |\{f'_{nk}\}_n|$. Next, the number of slowness-frequency pairs for each guided wave, which are expected at the final stage, are defined by the relation $M_k = M'_k - M^1_k - M^2_k$, where $M^1_k =]M'_k\delta_1[$ is the number of individual points to be excluded from initial set at random positions, while $M^2_k =]M'_k\delta_2[$ is the number of points in the chains or the sets of adjacent points of lengths from 2 to 7 to be deleted also at random positions. To obtain

$$\check{s}_k(\boldsymbol{\theta}^*, f_n) = \bigcup \left\{ s'_k(\boldsymbol{\theta}^*, f'_{n'k}) | n' \notin \mathcal{I}_k, n' \in \overline{1, M'_k} \right\},$$

the auxiliary set

$$\mathcal{I}_k = \left(\bigcup_{j=1}^{M^1_k} \left\{ \mathcal{A}_{kj} \right\} \right) \cup \left(\bigcup_j \left\{ \mathcal{B}_{kj} \right\} \right)$$

is composed of indices of slowness-frequency pairs to be deleted from the initially generated set $s_k(\boldsymbol{\theta}^*, f'_n)$ employing temporary sets

$$\mathcal{A}_{kj} = \text{random}(1, M'_k)$$

Preprints (www.preprints.org) | NOT PEER-REVIEWED | Posted: 18 April 2022 doi:10.20944/preprints202204.0161.v1

and

$$\mathcal{B}_{kj} = \left\{ b_{kj}, \ldots, b_{kj} + l_{kj} \right\},$$

where

$$b_{kj} = \text{random}(1, M'_k),$$
$$l_{kj} = \text{random}(2, 7),$$
$$\sum_j |l_{kj}| = M_k^2$$
$$\mathcal{A}_{kj} \bigcap \mathcal{A}_{kj'} = \mathcal{B}_{kj} \bigcap \mathcal{B}_{kj'} = \mathcal{A}_{kj} \bigcap \mathcal{B}_{kj'} = \emptyset, \qquad \forall j \neq j'.$$

The latter allows us to simulate data gaps and white noise that are usually observed in experimental data [11,20].

The sets $(\check{s}_k(\boldsymbol{\theta}^*, f_n), f_n)$ generated according to the procedure described above are employed further to analyse the behaviour of the proposed objective functions. Figure 4 shows four corrupted data sets $(\check{s}_k(\boldsymbol{\theta}^*, f_n), f_n)$ for two values of the standard deviation ($\sigma = 0.0025$ and $\sigma = 0.01$) and two levels of corruption ($\delta = 20\%$ and $\delta = 40\%$) for $\boldsymbol{\theta}^* = \{70\text{ GPa}, 0.33, 1.9\text{ mm}\}$.

6. Numerical analysis

6.1. Analysis of the properties of objective functions

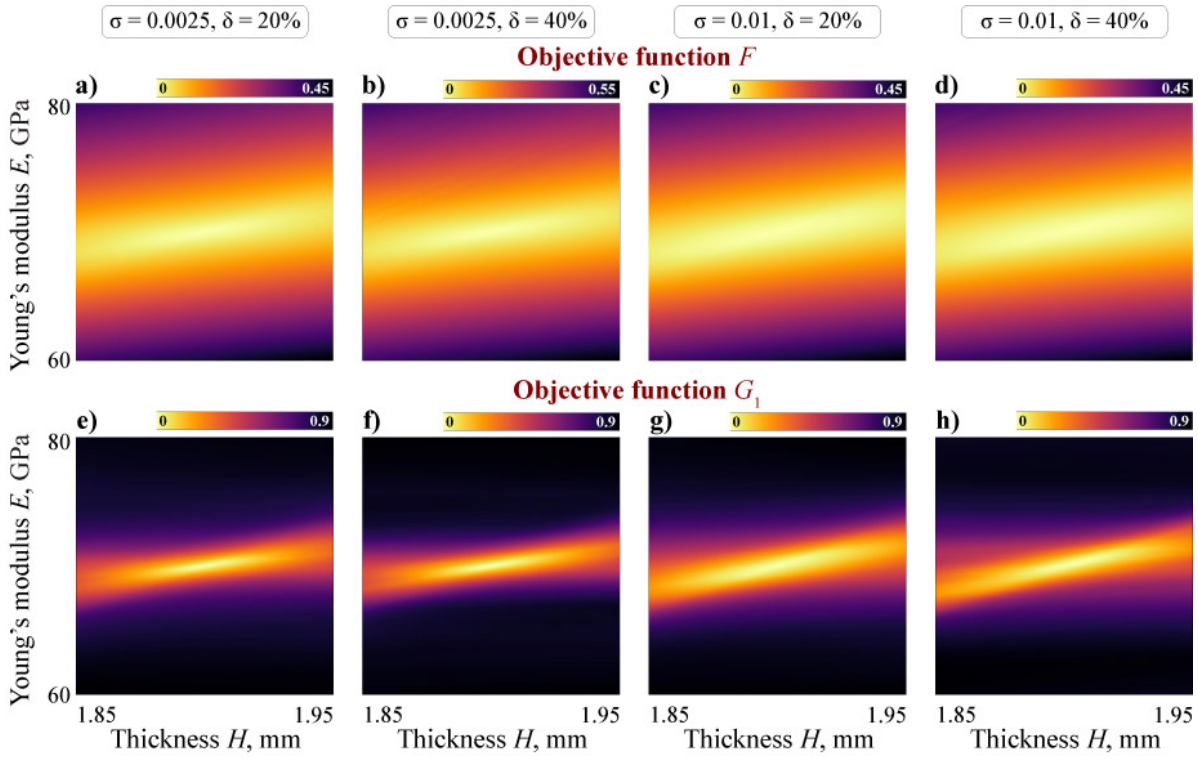

Figure 5. Surfaces of objective functions $F(\widetilde{\boldsymbol{\theta}})$ (a–d) and $G_1(\widetilde{\boldsymbol{\theta}})$ (e–h) at $\widetilde{\boldsymbol{\theta}} = (E, \nu = 0.33, H)$ and for different degrees of corruptness σ ($\delta = 0.4$).

For all the data samples depicted in Figure 4, the two-dimensional surfaces $f(E, 0.33, H)$, $f(E, \nu, 1.9\text{ mm})$ and $f(70\text{ GPa}, \nu, H)$ are depicted in Figures 6–5 as contour plots of three slices ($\nu = 0.33$, $H = 1.9$ mm and $E = 70$ GPa) calculated for two objective functions (F and G_1 are calculated for the corrupted data $\check{s}_k(\boldsymbol{\theta}^*, f_n)$ at $\sigma = 0.0075$ and $\delta = 20\%$). These figures demonstrate that the both objective functions are smooth, and the global minimum, which is clearly visible for both objective functions in Figures 6–5, could be

Preprints (www.preprints.org) | NOT PEER-REVIEWED | Posted: 18 April 2022 doi:10.20944/preprints202204.0161.v1

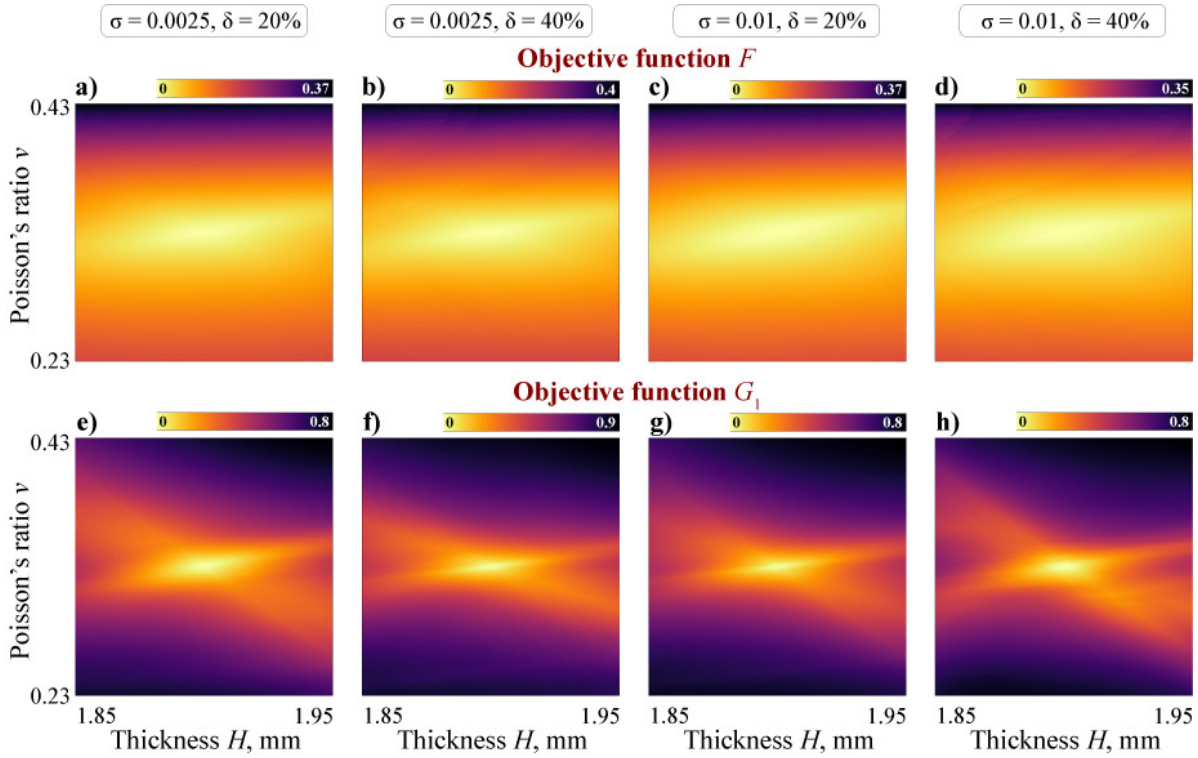

Figure 6. Surfaces of objective functions $F(\widetilde{\boldsymbol{\theta}})$ (a–d) and $G_1(\widetilde{\boldsymbol{\theta}})$ (e–h) at $\widetilde{\boldsymbol{\theta}} = (70\text{ GPa}, \nu, H)$ for different degrees of corruptness ($\delta = 0.4$).

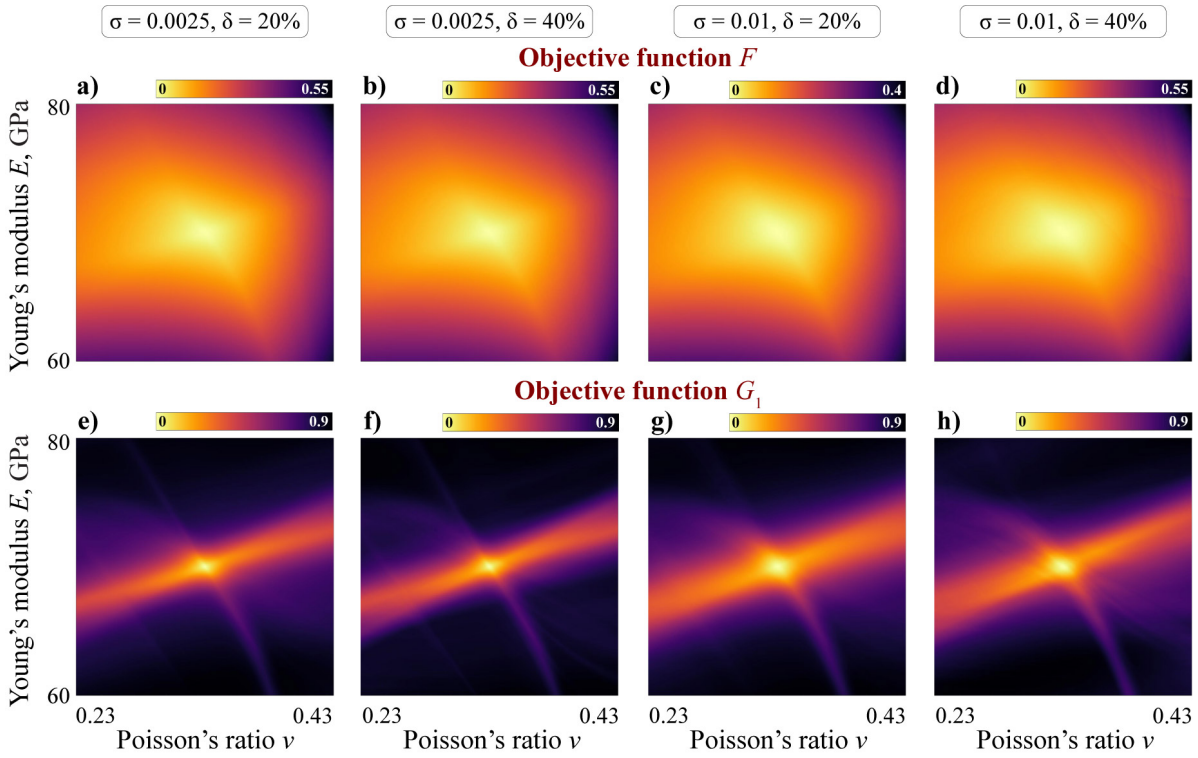

Figure 7. Surfaces of objective functions $F(\widetilde{\boldsymbol{\theta}})$ (a–d) and $G_1(\widetilde{\boldsymbol{\theta}})$ (e–h) at $\widetilde{\boldsymbol{\theta}} = (E, \nu, 1.9\text{ mm})$ for different degrees of corruptness σ ($\delta = 0.4$).

determined at the next stage, where the minimization problem is solved. One can also note that objective function F is usually smoother than G_1.

Preprints (www.preprints.org) | NOT PEER-REVIEWED | Posted: 18 April 2022 doi:10.20944/preprints202204.0161.v1

6.2. Inverse problem solution using synthesized data

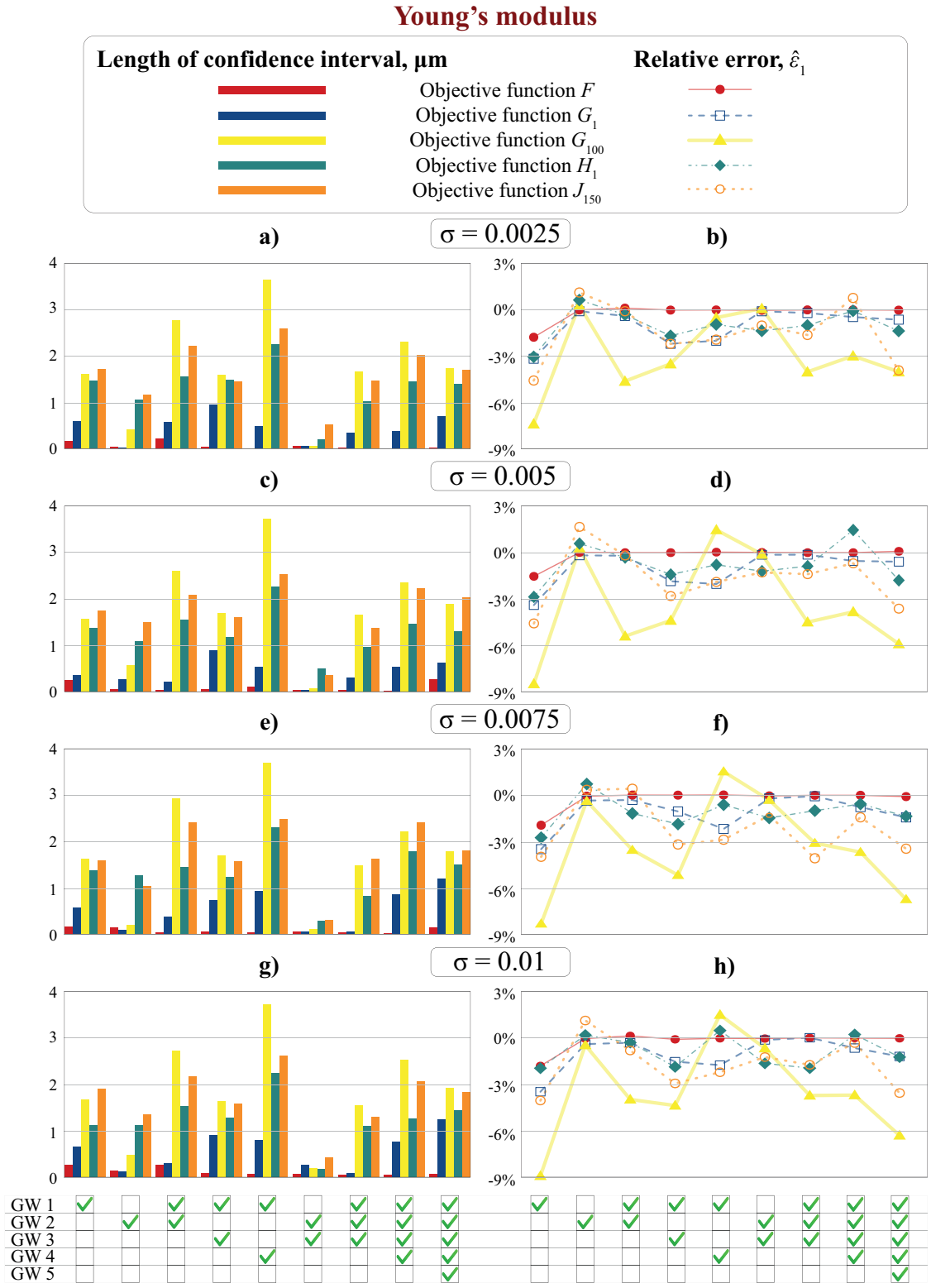

Figure 8. The length of confidence intervals (a,c,e,g) and the relative error $\hat{\varepsilon}_1$ (b,d,f,h) for Young's modulus E identification obtained using five objective functions $F, G_1, G_{100}, H_1, J_{150}$ for different levels of noise σ at $\delta = 40\%$.

Foremost, the material properties identification procedure has been validated using synthesized data $\breve{s}_k(\boldsymbol{\theta}^*, f_n)$ calculated for $\boldsymbol{\theta}^* = \{70\text{ GPa}, 0.33, 1.9\text{ mm}\}$ with different

Preprints (www.preprints.org) | NOT PEER-REVIEWED | Posted: 18 April 2022 doi:10.20944/preprints202204.0161.v1

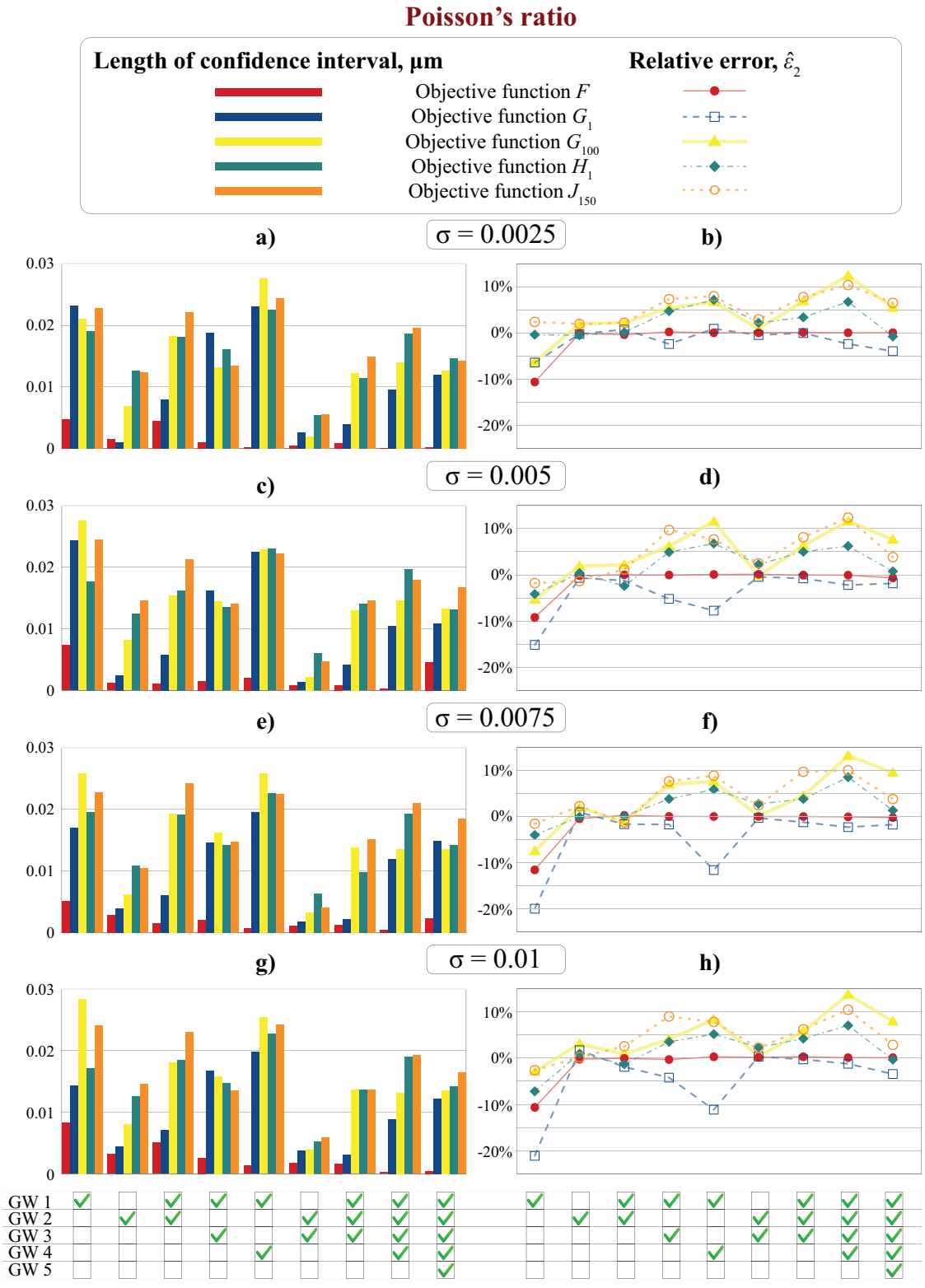

Figure 9. The length of confidence intervals (a,c,e,g) and the relative error $\hat{\varepsilon}_2$ (b,d,f,h) for Poisson's ratio ν identification obtained using five objective functions $F, G_1, G_{100}, H_1, J_{150}$ for different levels of noise σ at $\delta = 40\%$.

levels of noise σ and corruption $\delta = 40\%$. The statistics have been estimated for Young's modulus E, Poisson's ratio ν and plate thickness H using five different objective functions $F, G_1, G_{100}, H_1, J_{150}$ and the employing 1000 tests for synthesized data. Figures 8–10

Preprints (www.preprints.org) | NOT PEER-REVIEWED | Posted: 18 April 2022 doi:10.20944/preprints202204.0161.v1

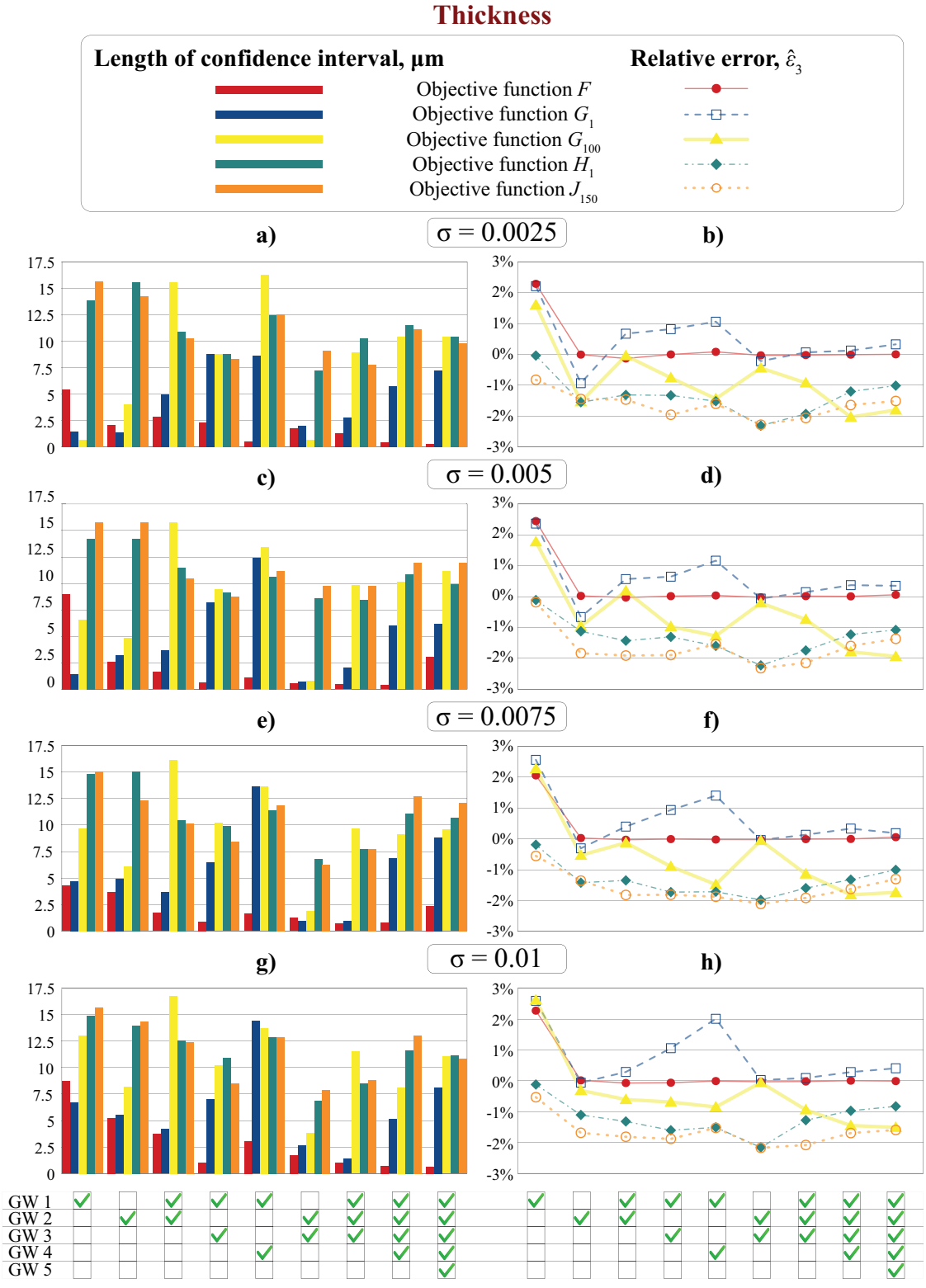

Figure 10. The length of confidence intervals (a,c,e,g) and the relative error $\hat{\varepsilon}_3$ (b,d,f,h) for plate thickness H identification obtained using five objective functions $F, G_1, G_{100}, H_1, J_{150}$ for different levels of noise σ at $\delta = 40\%$.

depicts the lengths of confidence intervals in subplots (a, c, e, g), whereas the relative error

$$\hat{\boldsymbol{\epsilon}} = \frac{\mathrm{E}(\hat{\boldsymbol{\theta}}) - \boldsymbol{\theta}^*}{\boldsymbol{\theta}^*}.$$

Preprints (www.preprints.org) | NOT PEER-REVIEWED | Posted: 18 April 2022 doi:10.20944/preprints202204.0161.v1

is illustrated in subplots (b, d, f, h). Here the mean of the parameter estimates $\hat{\boldsymbol{\theta}}$ is employed as an estimate for the expectation $\mathrm{E}(\hat{\boldsymbol{\theta}})$. The length of the confidence interval for the mean indirectly indicates the efficiency of the estimates, which characterizes the accuracy of the obtained parameter estimates and allows us to compare the objective functions from this point of view. The relative error vector $\hat{\boldsymbol{\epsilon}}$ can be used to consider a property such as biased or unbiased parameter estimates. To investigate the influence of the presence of guided waves, various combinations of guided waves has been considered (markers in the bottom of Figures 8–10 show which modes have been included in the data set).

According to Figures 8–10, one can conclude that the estimates of all parameters determined using the objective function F, which summarizes residuals in slownesses, are unbiased and the most efficient for all the considered combinations of guided waves except for GW 1. However, it should be noted that all estimates for the only first guided wave GW 1, which is the fundamental antisymmetric mode, are biased. The objective function G_β gives the more efficiency and less biased estimates for $\beta = 1$ than $\beta = 100$ for the majority of the considered synthesized data sets. Compared to the objective functions H_1 and J_{150}, the functional G_1 provides also more accurate estimates.

In general, it should be mentioned that the majority of the estimates calculated using the approach based on the Fourier transform of Green's matrix give an underestimated value of Young's modulus up to 9% (see Figure 8) and an overestimated value of the Poisson's ratio (more than 10%), see Figure 9. Thickness estimates are also more inclined to be underestimated, but the error varies in the 3% range (Figures 10). It is also noteworthy that the most efficient and less biased estimates for Young's modulus and Poisson's ratio are determined for GW 2 and GW 2–GW 3. This regularity can not be reported for the sample's thickness, however, the estimation error is small for all the considered combinations of GW modes. It should be also noted that the computational time for the approach based on the slowness residuals is **????** times smaller than for the approach based on the Fourier transform of Green's matrix.

6.3. Inverse problem solution using LDV experimental data

GW modes					Statistics			
1	2	3	4	5	2.5%	97.5%	50%	mean
					Young's modulus			
✓	✓				70.48489	71.08083	70.58092	70.61958
	✓	✓			71.91615	72.00113	71.95661	71.93506
✓	✓	✓	✓	✓	71.63346	72.06074	72.01541	71.93475
					Poison's ratio			
✓	✓				0.2814911	0.3088387	0.2851565	0.2868929
	✓	✓			0.3426350	0.345837	0.3443798	0.345837
✓	✓	✓	✓	✓	0.3498317	0.352299	0.3513940	0.3512925
					Thickness			
✓	✓				2.038286	2.045689	2.044301	2.043785
	✓	✓			2.019506	2.022150	2.020586	2.020512
✓	✓	✓	✓	✓	2.001522	2.014291	2.013035	2.010527

Table 1: The cumulative percentages and the mean for the results calculated using objective function F based on the slowness residuals.

At the final stage the proposed approaches have tested and validated using experimental data obtained using the LDV setup for an aluminium plate with known parameters $\nu = 0.35$**,** $H = 2.0$ mm **and** $E = 72$ GPa**.** Figure 11 depicts slownesses $(\check{s}_k(\check{\boldsymbol{\theta}}, f_n), f_n)$ obtained applying the MPM to the experimental data as circles. The

Preprints (www.preprints.org) | NOT PEER-REVIEWED | Posted: 18 April 2022 doi:10.20944/preprints202204.0161.v1

GW modes	Statistics			
1 2 3 4 5	2.5%	97.5%	50%	mean
Young's modulus				
✓✓	71.57257	71.61732	71.59928	71.60707
✓✓	69.31747	71.97177	71.95452	71.77478
✓✓✓✓✓	69.98659	72.75823	72.47230	72.20928
Poison's ratio				
✓✓	0.3130311	0.3199611	0.3156035	0.3164631
✓✓	0.2584863	0.3394943	0.3394111	0.3352184
✓✓✓✓✓	0.2730250	0.3862568	0.3508503	0.3454789
Thickness				
✓✓	2.050283	2.058020	2.056627	2.055417
✓✓	1.985751	2.081555	2.029845	2.029940
✓✓✓✓✓	2.008208	2.090551	2.030139	2.034077

Table 2: The cumulative percentages and the mean for the results calculated using objective function G_1 based on Green's matrix.

optimization procedure has been run 1000 times using for the BFGS method with various starting points uniformly distributed in $10 \times 10 \times 10$ grid in the parameter $\boldsymbol{\theta}$ space using both objective functions. The statistics obtained for the estimates $\hat{\boldsymbol{\theta}}$ calculated using objective function F based on the slowness residuals are given in Table 1, while the statistic estimations related to the objective function G_1 based on the Fourier transform of Green's matrix are presented in Table 2. In these tables, the boundaries of the intervals, where 95% of all calculated parameters are located, as well as the medians and means are given. The results presented in these tables have been computed for the following sets of modes: GW 1–GW 2, GW 2–GW 3 and GW 1–GW 5. The conclusions that can be drawn from the analysis of Tables 1–2 are consistent with the results obtained for synthesized data provided in Subsection 6.2. The parameter estimates found for the approach using slowness residuals are more accurate, since the lengths of confidence intervals are narrower. At the same time, the obtained values are slightly underestimated for Young's modulus and Poisson's ratio and slightly overestimated for the thickness for the mode set GW 1–GW 2. As the final estimate of the faithful parameters, both the median and the mean values can be taken, since their values are very close. For calculations by means of the approach based on Green's matrix, only the results obtained for the set of modes GW 1–GW 5 can be considered acceptable.

Figure 11 depicts the slownesses calculated as a solution of dispersion equation (7) for parameters estimated using the developed numerical routines (solid, dashed, dash-dotted lines), which are given in Tables 1–2. Four sets of slowness curves corresponding to $\hat{\boldsymbol{\theta}}$ determined using experimental data $(\check{s}_k(\check{\boldsymbol{\theta}}, f_n), f_n)$ and two approaches employing data for modes GW 1–GW 2 (dashed and thick solid lines) and GW 1–GW 5 (dash-dotted and thin solid lines) are demonstrated in Figure 11. A sufficient discrepancy between theoretical curves and the experimental data is clearly visible by eye for modes GW 1–GW 2. **For the full data set including information on modes GW 1–GW 5, both approaches have more or less similar difference with experimentally obtained slownesses, though the objective function F based on the slowness residuals provide material properties more close to the actual ones.**

7. Discussions

The proposed automated procedure is an attempt to summarize and extend the results of the researchers mentioned in the introduction as well as many others, who used guided waves for material properties characterization. The comparison of two

Preprints (www.preprints.org) | NOT PEER-REVIEWED | Posted: 18 April 2022 doi:10.20944/preprints202204.0161.v1

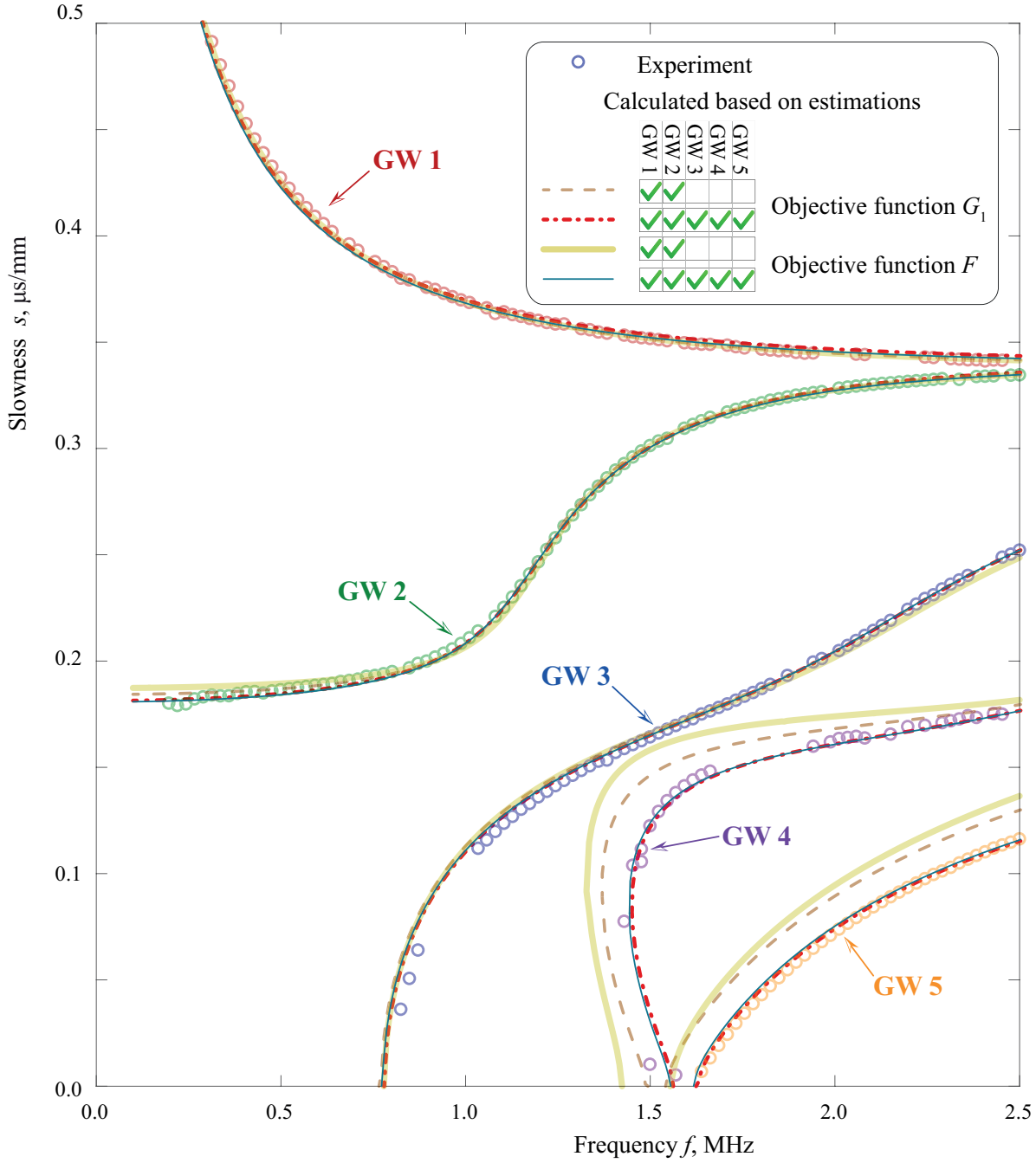

Figure 11. Experimentally observed (circles) and theoretically predicted slownesses (lines) calculated at $\hat{\theta}$ estimated using objective function F based on the slowness residuals (solid lines) and G_1 based on Green's matrix (dash-dotted and dashed lines) for GW 1–GW 2 (dashed and thick solid lines) and GW 1–GW 5 (dash-dotted and thin solid lines).

different approaches for objective function composition for the proposed procedure has shown that both approaches have some advantages as well as disadvantages. The approach using the Fourier transform of Green's matrix is much faster compared with the approach using discrepancy between slownesses. The authors believe that the advantages of the two approaches might be combined into an improved algorithm with low computational costs and accuracy close to the approach using slownesses. In this study, it was shown a sufficient influence of the number of propagating modes on the accuracy of the identification, which might be useful for improved algorithms based on both approaches considered in this paper.

Though the proposed procedure for material properties identification has been validated and verified for an elastic isotropic waveguide, it can be naturally extended for multi-layered structures and damaged laminates, e.g. considering the data from the previous authors' studies [11,20]. Another possible extension of the algorithm is the properties characterization of piezoelectric and anisotropic layered structures using information about the properties of guided waves propagating there. Besides, it is not limited by the matrix pencil method and laser Doppler vibrometry. The most important basis of the developed procedure is careful extraction of the information about dispersion characteristics of the layered waveguide and fast computational algorithms for Green's matrices, which have been recently advanced by the authors [27,28] and can be employed in near future.

Author Contributions: Conceptualization, M.V.G., O.V.D. and A.A.E.; methodology, M.V.G., O.V.D. and A.A.E.; software, M.A.A., O.V.D. and M.V.G; validation, I.A.B., O.V.D., M.A.A. and A.A.E.; formal analysis, O.V.D., M.V.G. and A.A.E.; investigation, O.V.D., M.V.G. and A.A.E.; resources, A.A.E. and M.V.G.; data curation, I.A.B., O.V.D., M.A.A. and A.A.E.; writing—original draft preparation, M.V.G., O.V.D. and A.A.E.; writing—review and editing, M.V.G., O.V.D. and A.A.E.; visualization, M.V.G. and O.V.D.; project administration, M.V.G.; project administration, M.V.G.; funding acquisition, M.V.G. All authors have read and agreed to the published version of the manuscript.

Funding: The research was carried out with the financial support of the Kuban Science Foundation in the framework of the project No. 20.1/118.

Institutional Review Board Statement: Not applicable

Informed Consent Statement: Not applicable

Data Availability Statement: Data sharing not applicable to this article as no datasets were generated or analyzed during the current study.

Acknowledgments: The authors are grateful to Professors E.V.Glushkov and N.V. Glushkova for valuable discussions. The authors express their deep gratitude to Prof. Rolf Lammering (Helmut Schmidt University, Hamburg, Germany) for the comprehensive support of the experimental investigations.

Conflicts of Interest: The authors declare no conflict of interest.

Abbreviations

The following abbreviations are used in this manuscript:

NDT	non-destructive testing
SHM	stuctural health monitoring
SCs	slowness curves
GWs	guided waves
LDV	laser Doppler vibrometer

References

1. Pagnotta, L. Determining elastic constants of materials with interferometric techniques. *Inverse Problems in Science and Engineering* **2006**, *14*, 801–818. doi:10.1080/17415970600838806.
2. Kam, T.; Chen, C.; Yang, S. Material characterization of laminated composite materials using a three-point-bending technique. *Composite Structures* **2009**, *88*, 624–628. doi:10.1016/j.compstruct.2008.06.015.
3. Tam, J.; Ong, Z.; Ismail, Z.; Ang, B.; Khoo, S. Identification of material properties of composite materials using nondestructive vibrational evaluation approaches: A review. *Mechanics of Advanced Materials and Structures* **2017**, *24*, 971–986. doi:10.1080/15376494.2016.1196798.
4. Ambrozinski, L.; Packo, P.; Pieczonka, L.; Stepinski, T.; Uhl, T.; Staszewski, W. Identification of material properties - Efficient modelling approach based on guided wave propagation and spatial multiple signal classification. *Structural Control and Health Monitoring* **2015**, *22*, 969–983. doi:10.1002/stc.1728.
5. Tam, J.H. Identification of elastic properties utilizing non-destructive vibrational evaluation methods with emphasis on definition of objective functions: a review. *Structural and Multidisciplinary Optimization* **2020**, *61*, 1677–1710. doi:10.1007/s00158-019-02433-1.

6. Chen, Q.; Xu, K.; Ta, D. High-resolution Lamb waves dispersion curves estimation and elastic property inversion. *Ultrasonics* **2021**, *115*, 106427. doi:https://doi.org/10.1016/j.ultras.2021.106427.
7. Okumura, S.; Nguyen, V.H.; Taki, H.; Haïat, G.; Naili, S.; Sato, T. Phase velocity estimation technique based on adaptive beamforming for ultrasonic guided waves propagating along cortical long bones. *Japanese Journal of Applied Physics* **2017**, *56*, 07JF06. doi:10.7567/jjap.56.07jf06.
8. Okumura, S.; Nguyen, V.H.; Taki, H.; Haïat, G.; Naili, S.; Sato, T. Rapid High-Resolution Wavenumber Extraction from Ultrasonic Guided Waves Using Adaptive Array Signal Processing. *Applied Sciences* **2018**, *8*. doi:10.3390/app8040652.
9. Bochud, N.; Laurent, J.; Bruno, F.; Royer, D.; Prada, C. Towards real-time assessment of anisotropic plate properties using elastic guided waves. *The Journal of the Acoustical Society of America* **2018**, *143*, 1138–1147. doi:10.1121/1.5024353.
10. Tian, Z.; Yu, L. Lamb wave frequency-wavenumber analysis and decomposition. *Journal of Intelligent Material Systems and Structures* **2014**, *25*, 1107–1123. doi:10.1177/1045389X14521875.
11. Golub, M.V.; Doroshenko, O.V.; Wilde, M.V.; Eremin, A.A. Experimental validation of the applicability of effective spring boundary conditions for modelling damaged interfaces in laminate structures. *Composite Structures* **2021**, *273*, 114141. doi:10.1016/j.compstruct.2021.114141.
12. Eremin, A.A.; Golub, M.V.; Wilde, M.V.; N., P.V. Influence of retroreflective films on the behaviour of elastic guided waves measured with laser Doppler vibrometry. *Measurement* **2022**. doi:10.1016/j.jsv.2018.10.015.
13. Takahashi, V.; Lematre, M.; Fortineau, J.; Lethiecq, M. Elastic parameters characterization of multilayered structures by air-coupled ultrasonic transmission and genetic algorithm. *Ultrasonics* **2022**, *119*, 106619. doi:https://doi.org/10.1016/j.ultras.2021.106619.
14. Lu, L.; Charron, E.; Glushkov, E.; Glushkova, N.; Bonello, B.; Julien, F.H.; Gogneau, N.; Tchernycheva, M.; Boyko, O. Probing elastic properties of nanowire-based structures. *Applied Physics Letters* **2018**, *113*, 161903. doi:10.1063/1.5045665.
15. Pagnotta, L.; Stigliano, G. Elastic characterization of isotropic plates of any shape via dynamic tests: Practical aspects and experimental applications. *Mechanics Research Communications* **2009**, *36*, 154–161. doi:10.1016/j.mechrescom.2008.09.003.
16. Wilde, M.V.; Golub, M.V.; Eremin, A.A. Experimental observation of theoretically predicted spectrum of edge waves in a thick elastic plate with facets. *Ultrasonics* **2019**, *98*, 88–93. doi:10.1016/j.ultras.2019.05.009.
17. Tu, J.H.; Rowley, C.W.; Luchtenburg, D.M.; Brunton, S.L.; Kutz, J.N. On dynamic mode decomposition: Theory and applications. *Journal of Computational Dynamics* **2014**, *1*, 391–421. doi:10.3934/jcd.2014.1.391.
18. Schöpfer, F.; Binder, F.; Wöstehoff, A.; Schuster, T.; von Ende, S.; Föll, S.; Lammering, R. Accurate determination of dispersion curves of guided waves in plates by applying the matrix pencil method to laser vibrometer measurement data. *CEAS Aeronautical Journal* **2013**, *4*, 61–68.
19. Chamaani, S.; Akbarpour, A.; Helbig, M.; Sachs, J. Matrix Pencil Method for Vital Sign Detection from Signals Acquired by Microwave Sensors. *Sensors* **2021**, *21*. doi:10.3390/s21175735.
20. Wilde, M.V.; Golub, M.V.; Eremin, A.A. Elastodynamic behaviour of laminate structures with soft thin interlayers: theory and experiment. *Materials* **2022**, *15*, 1307. doi:10.1016/j.jsv.2018.10.015.
21. Thelen, M.; Bochud, N.; Brinker, M.; Prada, C.; Huber, P. Laser-excited elastic guided waves reveal the complex mechanics of nanoporous silicon. *Nature Communications* **2021**, *12*. doi:10.1038/s41467-021-23398-0.
22. Liu, Z.; Xu, K.; Li, D.; Ta, D.; Wang, W. Automatic mode extraction of ultrasonic guided waves using synchrosqueezed wavelet transform. *Ultrasonics* **2019**, *99*, 105948. doi:https://doi.org/10.1016/j.ultras.2019.105948.
23. Fairuschin, V.; Brand, F.; Backer, A.; Drese, K.S. Elastic Properties Measurement Using Guided Acoustic Waves. *Sensors* **2021**, *21*. doi:10.3390/s21196675.
24. Lan, B. Non-iterative, stable analysis of surface acoustic waves in anisotropic piezoelectric multilayers using spectral collocation method. *Journal of Sound and Vibration* **2018**, *433*, 16–28. doi:https://doi.org/10.1016/j.jsv.2018.07.007.
25. Grünsteidl, C.; Murray, T.W.; Berer, T.; Veres, I.A. Inverse characterization of plates using zero group velocity Lamb modes. *Ultrasonics* **2016**, *65*, 1–4. doi:https://doi.org/10.1016/j.ultras.2015.10.015.
26. Eremin, A.; Glushkov, E.; Glushkova, N.; Lammering, R. Evaluation of effective elastic properties of layered composite fiber-reinforced plastic plates by piezoelectrically induced guided waves and laser Doppler vibrometry. *Composite Structures* **2015**, *125*, 449–458. doi:http://dx.doi.org/10.1016/j.compstruct.2015.02.029.
27. Fomenko, S.I.; Golub, M.V.; Doroshenko, O.V.; Wang, Y.; Zhang, C. An advanced boundary integral equation method for wave propagation analysis in a layered piezoelectric phononic crystal with a crack or an electrode. *Journal of Computational Physics* **2021**, *447*. doi:10.1016/j.jcp.2021.110669.
28. Glushkov, E.; Glushkova, N.; Eremin, A.; Lammering, R. Group velocity of cylindrical guided waves in anisotropic laminate composites. *Journal of Acoustical Society of America* **2014**, *135*, 148–154. doi:10.1121/1.4829534.